Structure and Charge Transport Properties of CycloParaPhenylene monolayers on Graphite

Pérez-Guardiola, A.[a], Pérez-Jiménez, Á. J.[a],
Muccioli, L.*[b], and Sancho-García, J. C.†[a]

[a]Departamento de Química-Física, Universidad de Alicante,
E-03080 Alicante, Spain
[b]Department of Industrial Chemistry "Toso Montanari",
Viale Risorgimento 4, 40136 Bologna, Italy

February 6, 2019

*luca.muccioli@unibo.it
†jc.sancho@ua.es

Abstract

We theoretically investigate, by means of atomistic molecular dynamics simulations employing a tailored and benchmarked force field, the nanoscale organization of cycloparaphenylene molecules when physisorbed on a graphite surface. The landing of a single molecule is first considered, to progressively deposit more molecules to finally reach the full coverage of the surface. This protocol allows to study, consequently, the mechanism and structural pattern of their self-aggregation. The interfacial morphologies obtained are then analyzed in terms of the electronic coupling between neighboring molecules, allowing thus to provide information about the associated charge-transfer phenomena which could take place in these highly organized monomolecular layers.

1 Introduction

[n]CycloParaPhenylenes (CPPs) molecules are synthesized by sequentially linking phenyl units in 1,4 position to form a macrocycle (see Fig. 1). These non-planar cyclic π-conjugated systems have largely attracted the attention of theoretical and experimental groups, due to their unique electronic and optical properties and potential applications in Organic Electronics.[1,2] In fact, these systems present variable emission spectra and quantum yields as a function of their size, in contrast with linear analogues.[3] For instance, [10]CPP and some tetraalkoxy derivatives were used very recently to prepare thin-films in order to investigate their properties as electron-transport materials.[4] In the field of supramolecular chemistry, [10]CPP is able to form a supramolecular concave-convex π-stacking complex with C_{60} fullerenes in solution[5] and solid-state,[6] which can be further exploited to realize self-assembled functional materials. [n]CPPs can also be viewed as the smallest cross-section of an arm-chair single-walled carbon nanotube (SWCNT) and have thus a potential use as building blocks for the *bottom-up* synthesis of well defined SWCNT with specific edges and size.

The synthesis of CPPs has been experimentally challenging due to the strain energy needed to close the ring.[7] Vögtle et al.[8,9] attempted to synthesize CPPs from macrocycles formed by arene and cyclohexane units to therefore reduce the strain energy of the system. However, the first synthesis of CPPs was afforded only by Jasti et al.[10] in 2008, followed by the first selective synthesis of CPPs by Itami et al.[11,12] using a modular approach to build [n]CPPs with n$\geq$12. Other successfully strategies (Yamago et al.[13]) use a square-shaped tetra platinum biphenyl complex as an intermediate to selectively synthesize the [8]CPP molecule. In the above mentioned works, it was possible to obtain CPPs in the milligram-scale, with Jasti et al.[6,14] producing the first gram-scale synthesis. The smallest CPP synthesized up to day is [5]CPP,[15] which shows the great success achieved so far in overcoming the strain energy.

Concerning the supramolecular packing, the solid-state (3D) structure of CPPs

has been characterized in several works by means of X-ray diffraction.[16,17] The molecules self-assemble in a herringbone pattern independently of their size, as it often happens for other π-conjugated systems. An exception is the [6]CPP case, for which three different polymorphs have been found up to date. The first solid-state characterization of [6]CPP revealed a tubular-like structure,[14] but a recent study revealed that the crystallographic structure might depend on the crystalization conditions, finding also a herringbone configuration a few of kcal/mol more stable than the tubular one.[18] More recently, another polymorph of [6]CPP has been found when the crystallization is carried out by sublimation at 220° C. In these conditions, no solvent molecules are occluded inside the [6]CPP cavity, and thus, a concave-convex structure appears (i.e. molecules tightly packed in a T-like shape minimizing the internal space inside the cavities).[19]

These findings clearly reveal the subtle yet dominant effect of the weak intermolecular interactions driving the supramolecular self-assembly of these systems. Motivated by this, some of us investigated in a previous theoretical work the adsorption energies of [8]CPP on small carbon nano-flakes (circumcirmcumcoronene) and how these through-space weak-forces can serve to inmobilize the systems in energetically favored configuration.[20] In the present study, we wish to go a step further and employ a tailored force field and Molecular Dynamics (MD) simulations to predict the supramolecular structure of thin films of CPPs on graphite surfaces. The systematic exploration of the adsorption preferences, together with the effect of structural and thermal disorder, also allows us to disclose the associated charge-transport magnitudes, rates and mobilities, thus revealing key structure-property relationships at the nanoscale.

2 Computational details

2.1 Adsorption energy profiles

Energy profiles for the absorption of [8]CPP on the graphite surface have been calculated using the HF-3c (HF/minix-gCP-D3)[21] method, which has been demonstrated to be close to the accuracy of DFT-D3 (dispersion-corrected Density Functional Theory) with large basis sets or to MP2 (Møller-Plesset perturbation theory at second-order) calculations at the complete basis set limit, for the sublimation enthalpies of organic crystals.[22] The HF-3c method combines a Hartree-Fock calculation employing a minimal basis set, with different corrections to explicitly account for the missing dispersion interactions, basis sets incompleteness effects, and the tendency to calculate too short covalent bonds between chemical species. The ORCA 3.0.3 package[23] was used for this purpose.

2.2 Molecular Dynamics simulations

Partial atomic charges for the [8]CPP molecule were computed at the B3LYP/cc-pVTZ//B3LYP/6-31G*[24–26] level, employing Gaussian09 D.01,[27] by their fitting to the electrostatic potential.[28] For the Force Field (FF) simulations, 1-4 intramolecular interactions were scaled by a factor of 5/6 for the case of electrostatic and 1/2 for Lennard-Jones (LJ) interactions, typical of the AMBER family of force fields.[29] A cutoff of 18 Å was adopted for the evaluation of the LJ interactions, and fully periodic electrostatics was included by using the smooth Particle Mesh Ewald (PME)[30] method with a grid spacing of 1.5 Å. The FF fine-tuning is discussed in detail in section 3.1. A timestep of 1 fs was used and non-bonded and full electrostatics were evaluated each 2 fs. Velocities were rescaled to a specific temperature each 1 ps during simulations. For simulations in the NPT ensemble (e.g. [8]CPP crystal simulation), the Berensend barostat[31] was employed with a target pressure of 1 atm (1.01325 bar). Atomistic molecular dynamics simulations were carried out employing the NAMD 2.11 package.[32]

2.3 Definition of the [8]CPP tridimensional crystal and the graphite surface

Experimental data for the crystalline structure of [8]CPP was obtained from the literature.[6] The unit cell dimensions are $a = 12.933$ Å, $b = 8.010$ Å, $c = 19.368$ Å, $\alpha = \gamma = 90°$, $\beta = 105.363°$, the cell containing two [8]CPPs. A supercell of 432 units of [8]CPPs has been created replicating the unit cell (6×6×6). Cristallographic data for graphite were also obtained from literature.[33] The dimensions of the graphite crystal cell are $a = b = 2.470$ Å, $c = 6.790$ Å, $\alpha = \beta = 90°$ and $\gamma = 120°$, and the unit cell contains two layers of two atoms each. The interlayer separation is fixed to $c/2$ Å. A rectangular eight-atom cell was created from the hexagonal graphite unit cell, with dimensions $a = 2.470$ Å, $b = a\sqrt{3} = 4.278$ Å, $c = 6.790$ Å, $\alpha = \beta = \gamma = 90°$. A minimal model of the graphite surface and its corrugation was realized with two carbon layers. The bottom layer was frozen during the simulations to avoid the graphite surface to bend due to the small thickness of the simulated surface. Conversely, the atoms of the top graphitic layer were allowed to change their nuclear coordinate during molecular dynamics simulations. In all simulations, conducted by employing 3D periodic boundary conditions, the vertical side of the box, corresponding to the direction normal to the graphite surface, was fixed to 10 nm to allow enough vacuum space between the periodic graphite surface replicas.

For the adsorption of isolated CPPs, and the corresponding self-aggregation on the surface, a graphite surface of dimensions $a = 98.800$ Å, $b = 98.394$ Å, $c = 100.000$ Å (40×23×1 replicas of the graphite rectangular cell mentioned above) was used. For the full-coverage studies, the graphite dimensions were chosen to minimize the mismatch between the adlayer and the graphite. Two stable adlayer structures were found and, as a consequence, two graphite surfaces were prepared with dimensions: i) $a = 113.620$ Å, $b = 98.394$ Å, $c = 100.000$ Å (46×23×1) for the hexagonal structure; and ii) $a = 64.220$ Å, $b = 59.892$ Å, $c = 100.000$ Å (26×14×1) for the herringbone structure, respectively.

2.4 Charge-transfer parameters

The rate of electron transfer is described in the framework of the Fermi's Golden Rule; assuming the Franck-Condon approximation and the high-temperature regime (when the vibrational modes can be treated classically) the charge transfer rate is given by the semiclassical Marcus expression:[34–38]

$$k = \frac{2\pi}{\hbar}|t_{ab}|^2 \frac{1}{\sqrt{4\pi\lambda k_B T}} \exp\left(-\frac{(\lambda + \Delta G^{\ominus}_{ab})^2}{4\lambda k_B T}\right), \tag{1}$$

where $|t_{ab}| = \left|\left\langle \psi_b|\hat{H}|\psi_a \right\rangle\right|$ is the electronic coupling between the initial and final states. Other terms are λ, the reorganization energy, and $\Delta G^{\ominus}_{ab}$, the change in free energy (zero for systems of identical molecules in absence of applied voltage, like in the present case). $\hbar$ and k_B are fundamental constants, and T is the temperature (fixed here at 300 K). Whereas λ, the energy needed to charge/discharge the molecule during the charge migration (λ_h=281 meV and λ_e=302 meV), was calculated for isolated [n]CPP systems on Ref. [39], $|t_{ab}|$ depends of the relative position, orientation and internal degrees of freedom of the monomers in a dimer configuration extracted from the supramolecular assembly. Traditionally, this term was approximated to half the energy between both initial and final states in a single calculation of the dimer, but this approximation has been demonstrated to be inaccurate due to polarization effects. The approach used here was proposed by Valeev et. al.,[40] projecting the molecular orbitals of the dimer on the basis of the molecular orbitals of the individual molecules. This approach has been demonstrated very effective to calculate the electronic coupling in a variety of situations.[41,42] However, the Hamiltonian in the new orbital basis lacks the orthonormalization condition and thus a Löwdin's orthonormal transformation[43] is needed. Therefore, the explicit expression for t_{ab},[44,45] also referred here as Charge Transfer Integral (CTI), is defined in terms of the non-orthonormal Hamiltonian as:

$$t_{ab} = \frac{\widetilde{t}_{ab} - \frac{1}{2}(\widetilde{e}_a + \widetilde{e}_b)S_{ab}}{1 - S^2_{ab}}, \tag{2}$$

where $\widetilde{t}_{ab}$ is the off-diagonal element between states a and b (e.g HOMO of both monomers for hole tranfer), $\widetilde{e}_a$ and $\widetilde{e}_b$ are the on-site energies and S_{ab} is the overlap.

ωB97X/DZP[46] calculations, using the ORCA 3.0.3 package,[23] were carried out to obtain the Hamiltonian and overlap in the atomic orbital basis. Note that the use of this functional overcomes the density-functional dependence on calculated transfer integrals.[47]

The corresponding mobilities for holes and electrons are calculated from the diffusion coefficient:

$$\mu = \frac{q}{k_B T} D, \tag{3}$$

which is in turn determined by the following equation:

$$D = \frac{1}{2} \sum_i (\vec{r_i} \cdot \vec{e})^2, \tag{4}$$

with k_i the calculated charge-transfer rate, the sum runs over all the neighbours in a perfect lattice, $\vec{r_i}$, is the inter-neighbour distance, and $\vec{e}$ orientation along which the mobility is calculated.[48]

2.5 Visualizers and other tools

The UCSF-Chimera program[49] was used for the visualization of molecules and the Mercury 3.10.3 program[50] for the visualization of crystallographic data. The VMD[51] tool was employed for the representation of the molecular dynamics simulations snapshots. All other graphics were prepared using matplotlib 2.2.2 python module.[52]

3 Results and discussion

3.1 Force Field parameterization

For the study of [8]CPP and its self-aggregation process on graphitic surfaces employing atomistic simulations, we first developed a force-field able to reproduce the involved non-bonded intermolecular interactions, motivated by previous studies[20]

of the energy profile of [8]CPP interacting with finite-size graphene surfaces (circumcoronenes and circumcircumcoronenes). Linear para-phenylenes were formerly studied by Olivier et al.[53] employing the AMBER-OPLS force field,[54] with scaled parameters for the non-bonded interactions and refitted torsional energy profiles to reproduce p-quinquephenyl phase behavior. Not surprisingly, since it was parameterized to reproduce the density of quinquephenyl nematic phase at 660 K, Olivier's force field[53] is not able to closely reproduce the quantum-chemical results for the intermolecular interactions of our system with surfaces, and we thus carried out a new optimization of the Lennard-Jones (LJ) parameters to fit the adsorption curves previously calculated at the HF-3c level. To obtain a more accurate description near the minimum of the curves, the points were weighted using a Boltzmann distribution at a temperature of 1000 K. The optimized LJ parameters for the atoms types defined in Figure 1 are $\epsilon_{_C} = -0.090$ kcal/mol, $\sigma_{_C} = 1.860$ Å, $\epsilon_{_H} = -0.061$ kcal/mol, $\sigma_{_H} = 1.300$ Å, $\epsilon_{_{C-H}} = -0.086$ kcal/mol, and $\sigma_{_{C-H}} = 3.070$ Å.

Concerning the conformation of [8]CPP, the dihedral angle formed between two connected phenyl rings, using the torsional parameters from Ref. [53], is predicted to be 31.6° compared with the value of 30.8° at the B3LYP/6-31G* level. The dihedral angle for the linear oligomers is around 40°,[55] with smaller values here due to the cyclic topology.[56] We can thus conclude that the tailored FF is able to also reasonable reproduce the geometrical shape of single [8]CPP molecules, and thus intra- and inter-molecular structural features relevant for the aggregation process.

Figure 2 clearly shows that the results from our tuned force field are in good agreement with the energy profiles at the HF-3c level of theory. The main contributions to the curve 2a are C–H and C–C interactions, with the former in minor proportion. Curve 2b includes a larger contribution of C–C interactions, while curve 2c also includes a small contribution from H–H together with the C–C and C–H interactions. In curve 2d, the molecule at that particular relative orientation, is rotated to explore the roughness of the graphite surface, which could play an important role in the 2D translational diffusion of these molecules. Small differences between HF-3c

and FF energies are found in the vicinity of the minimum, with the main ones being located at distances shorter than the minimum, where the repulsive part of the potential is predominant. The mean average error for all the curves is 1.80 kcal/mol, and it is largely originated from the fitting of the rotational profile in the curve 2d, for which the agreement is not quantitative (for instance HF-3c predicts a barrier of 3.4 kcal/mol and the FF of 2.6 kcal/mol). Despite that, the elsewhere small error between the HF-3c curves and the FF demonstrate that the force field can reasonably describe the energetics of aggregation and adsorption on graphite.

3.2 Force field benchmarks

As a further test, a comparison between quantum chemistry and molecular mechanics intermolecular energies was performed for the most important interacting dimers extracted from the experimental crystalline structure of [8]CPP.[6] These dimers were not part of the training set used for the parameterization of our force field and they thus serve to test its ability to reproduce the binding energies of [8]CPP in different situations. Note also that these dimers are those contributing the most to the crystalline cohesive energy of the [8]CPP system. In Table 1, B3LYP-D3(BJ)/cc-pVTZ[57] interaction energies previously computed[58] are compared with HF-3c and FF energies. Note that HF-3c underestimates by 10-17% the interaction energies provided by the B3LYP-D3(BJ) method, in line with previous applications to interaction energies and crystal structures of organic molecules,[6] but it allows a much faster screening of the non-covalently bound systems shown in Figure 2. The interaction energies calculated with molecular dynamics force fields are very similar to the HF-3c ones and slightly better in the comparison with DFT values, showing that the parameterization is robust.

The crystalline structure of the [8]CPP was simulated at a temperature of 300 K and 1 atm of pressure for 10 ns (see simulation details in 2.2). Equilibration was reached in the very first picoseconds. The results in Table 2 show that the box dimension reduce a 2% its volume compared with the experimental structure. This

small disagreement between simulated and experimental structure is normally acceptable and in line with previous reports for organic crystals.[59]

3.3 Structural analysis

3.3.1 Adsorption of isolated CPP on the surface

We explored first the interactions of a single molecule of [8]CPP on the graphite surface via molecular dynamics simulations. The adsorption of a single molecule was studied for two different orientations: the first one is shown in Fig. 2a, referred hereafter as horizontal configuration (HC), and the second is shown in Fig. 2b, called vertical configuration (VC). Simulations for 40 ns at different temperatures (e.g. 50, 100,. . . , 400 K) were carried out. The vertical configuration turned out to be unstable at any temperature. The molecule moves on the surface in its original configuration only for a short time ($\sim$1 ns) before collapsing in the horizontal configuration. The reason for this instability can be explained in terms of the interaction energy profiles shown in the Figs. 2a and 2b. The HC stabilization energy is in fact more than twice the VC stabilization energy, and thus the system spontaneously evolves to a HC. Even slightly larger stabilization of the HC configuration with respect to the VC might be obtained considering a thicker graphitic surface.

3.3.2 Self-aggregation process

The study of the self-aggregation of CPPs on the HC configuration was performed with an increasing number of molecules N^2 (N = 2–7) in the simulation box. The molecules were disposed on the surface with their center of mass lying on a perfect 2D lattice and with dimensions a/N and b/N, where a and b are the sides of the simulation box. Then, a MD simulation at 200 K was carried out for 10 ns. The diffusion of molecules over the surface is required to observe spontaneous aggregation, which for our system becomes significant only at temperatures above 150-200 K.

All the simulations showed some degree of molecular aggregation: the molecules

form nanoislands possessing a hexagonal structure with a mean distance between their center of mass of 14.2 Å. At low coverages (i.e. $N^2 = 2^2$ and 3^2) free molecules diffuse and aggregate to form a single cluster. At higher coverages (i.e. 4^2), all molecules form first small clusters in few ps, that subsequently migrate and merge. Aggregates larger than about 10 molecules hardly diffuse on the surface, and at the highest coverages (i.e. 5^2, 6^2 and 7^2), the density of molecules is so high that the aggregation occurs after the very few picoseconds from the beginning of the simulation. We also calculated the stabilization energy per molecule in the cluster using the following expression:

$$\Delta E_{(i)} = E_{CPP(i)-Surface} + \frac{1}{2}\sum_{j} E_{CPP(i)-CPP(j)}, \tag{5}$$

where the $E_{CPP(i)-Surface}$ is the interaction energy of the CPP molecule with the surface and $E_{CPP(i)-CPP(j)}$ is the interaction energy of the target CPP molecule with its neighbors. The mean value for a molecule in the adlayer, when the six nearest-neighbors are considered, is −73.1 kcal/mol. Note that adsorption energy of a single molecule with the graphite surface is −56.1 kcal/mol, hence, aggregation in the horizontal configuration brings an enthalpic stabilization of about 17 kcal/mol.

The aggregation studies of monolayers in the VC was not explored in detail due to the relative instability (i.e. compare Figs. 2a and 2b) of a single molecule adsorbed in that configuration described above. Nonetheless, a possible monolayer structure with molecules in the VC was tested as a proof of concept. The proposed structure has been extracted from the experimental crystal, choosing the plane with the biggest stabilization energy (i.e the (1 0 $\bar{1}$) plane, see Table 1a), forming a herringbone (HB) structure: a rectangular cluster of 48 molecules with initial dimensions 6.096×6.408 nm (which corresponds to a 3×8 replica of the herringbone unit cell) adsorbed on the graphite layer. The adsorption energy in the HB structure is now −55.4 kcal/mol, compared with the value of −73.1 kcal/mol found in the hexagonal structure, but the stabilization energy per unit area is instead larger for the HB packing, being −41.9 kcal/nm^2 for the hexagonal structure and −68.1 kcal/nm^2 for

the herringbone one. The $E_{CPP(i)-surface}$ term is now -22.9 kcal/mol, which thus implies -32.5 kcal/mol of stabilization with its neighbors. We followed the evolution of this herringbone cluster during 10 ns at a temperature of 200 K and, as it was also expected, it proved to be unstable. At very short simulation times, some molecules at the borders of the cluster collapse in the HC. In addition, the crystalline packing, present in the initial configuration, is lost. In the next section we will further discuss the instability of this configuration.

3.3.3 Full-coverage

For the full-coverage simulations, the dimensions of the simulation box have been chosen to minimize the mismatch between the dimensions of the graphite and the adlayer. In the case of the hexagonal structure, see Fig. 3a, a simulation box containing 64 molecules were created from a rectangular unit cell with dimensions a=14.203 Å and b=24.599 Å replicated 8×4 over a rectangular graphite surface of dimensions A=113.62 Å and B=98.394 Å (temperature of 300 K during 10 ns).

Several attempts to stabilize the HB structure on surface have been made, although, in all cases, the herringbone configuration was lost in a few ps, probably also because the initial packing is not optimal since is extracted from the bulk crystal structure by removing the interactions with CPPs in other crystallographic directions. For this reason, in order to optimize the packing of an adlayer composed by molecules in the vertical configuration, and starting from the HB structure mentioned before, we applied an external pressure of 1 atm to the system in the plane direction. To avoid the molecules to go out of the plane, their positions were restricted to move in the directions inside the plane by adding a harmonic potential to the out-of-plane displacement. This strategy was successful and finally a (meta)stable crystalline structure was obtained. The main difference between the experimental crystalline HB arrangement in the bulk and the new structure found is that the HB interactions, labelled as $\mathbf{v}_2$ in Table 1, involve pairs of molecules with non-orthogonal ring planes and stacked in a convex-concave (CC) disposition (see Fig. 3b). A similar

configuration has been very recently reported by Spisak et. al.[19] for [6]CPP crystals growth by sublimation and deposition. The area of the new structure is a 21% less than the area of the original HB structure. This configuration is not observed in the simulation of the tridimensional crystal, that preserves the HB structure shown in Table 1, a result that we attribute to key interactions with neighbors in other crystallographic directions, that stabilize the HB orthogonal configuration and prevent possible solid state phase transitions from one polymorph to another.

Finally, a simulation with the new 2D structure fully covering the graphite surface was performed. The simulation box, with dimensions A=64.220 Å and B=59.892 Å, contains 60 molecules in the new configuration (rectangular unit cell with dimensions of a=12.844 Å and b=9.982 Å and 5×6 replicas). The stabilization energy per molecule for the new structure, see Eq. (5), is found to be −63.0 kcal/mol per molecule, corresponding to an energy per area unit of −98.2 kcal/nm^2, hence much larger than the one obtained for the orthogonal HB disposition. The in-plane radial distribution function in Figs. 3c and 3d shows that both the hexagonal and the second concave-convex structure preserve their crystalline order on graphite, and allows for a direct measurement of the lattice parameters ($a = 14.2$ Å for hexagonal, and $a = 12.86$ Å and $b = 9.88$ Å for the concave-convex configuration).

3.4 Charge-transfer integrals

3.4.1 The [8]CPP model system

We next investigated how the supramolecular packing can affect the electronic coupling between a pair of neighboring molecules, which critically depends on the intermolecular distance and orientation. The point group symmetry of [8]CPP in vacuum is D_{4d} with an alternation of the dihedral angles between phenylene units of 31.6° (angle predicted with the tailored FF). For the purpose of calculating the corresponding charge-transfer integrals (CTI) according to Eq. (2), a model dimer of [8]CPP (each monomer keeping a D_{8h} point group) was created and some typical configurations explored, translating and rotating one of the molecules. In Fig. 4 we show the evolution

of the CTI values corresponding to all the configurations explored in the current work.

The dimeric configurations shown in Fig. 4 have been systematically built as follows: i) two molecules were aligned with both C_8 axes in parallel. Then, one molecule was translated in a direction perpendicular to the C_8 axis and the two molecules rotated around their C_8 axis to place two phenyl rings in a face-to-face configuration. This configuration is called cofacial configuration. We explored the charge transport integrals in that configuration as a function of the intermolecular distance (see Fig. 4a); ii) starting from the cofacial configuration described above, both molecules were kept fixed at an arbitrary yet model distance of 14.7 Å and we then explore angular configurations rotating one molecule around its C_8 axis (see Fig. 4b); iii) again, starting from the cofacial configuration at an initial fixed distance of 14.7 Å, we explored the CTI when coplanarity is lost by moving one molecule along the direction of the C_8 axis (see Fig. 4c); iv) starting with the molecules oriented with the C_8 direction in parallel, one of the molecules was placed on top of the other at an initial distance of 6 Å. This configuration receives the name of tubular configuration. Then, we moved the top molecule in the C_8 direction (see Fig. 4d); v) in the tubular configuration at a fixed distance of 6.7 Å in the C_8 direction, the top molecule was displaced from the perfect tubular configuration, translating it in a direction perpendicular to the C_8 direction (see Fig. 4e); vi) the molecules were reoriented keeping the C_8 axis perpendicular, and placing one molecule (the so-called "T" or herringbone configuration) at the fixed distance of 10.0 Å in the C_8 direction with respect of the molecule in the bottom, to finally translate the molecule in the top along its C_8 direction (see Fig. 4f).

Interestingly, both hole and electron transfer integrals present similar magnitudes in Figs. 4a, 4b and 4c, contrarily to what is found in the tubular configurations in Figs. 4d and 4e, where electron transfer integrals are one order of magnitude larger than hole transfer integrals. The herringbone configuration shown in Fig. 4f presents electron and hole transfer integrals of similar magnitudes, although slightly bigger values are found again for the electron case. As expected, Figs. 4a and 4d show an exponential decay of values as a function of the distance, due to the loss of over-

lap between the two π-systems. The relative orientation of molecules is also critical for the understanding of electronic coupling values.[60] If we fix now our attention to Fig. 4e, t_e is favorable for a perfectly tubular configuration while a displacement of 2 Å produces a dramatical decrease of electron transport. In Fig. 4b, a rotation of $\sim$11° ($2\pi/32$ rad) is enough to reduce the hopping (t_h) to a value lower than 1 meV.

These results can be qualitatively rationalized from the shape of the HOMO and LUMO orbitals for a single [8]CPP molecule (see Fig. 5). For instance, in the HOMO level, the lobes of orbitals show a node every half phenyl monomer unit (see Fig. 5a) which translates to the behavior of electronic coupling values displayed in Fig. 4b. The largest electronic coupling arise from the bonding or antibonding combinations of these orbitals in a dimer configuration. Another situation where the global overlap between the involved molecular orbitals becames key is for the perfect tubular orientation (see Fig. 4d). As can be seen in Fig. 5, unlike the HOMO which is localized on the phenyl carbon atoms, the LUMO level presents lobes at the H-edges, which translates to a dominant overlap in the LUMO level of the dimer, helping to explain the discrepancies between t_e and t_h for that case.

3.4.2 Extension to monolayers

CTI were subsequently evaluated in the adlayers. For both studied structures, all unique dimers (192 and 240 for hexagonal and concave-convex, respectively) found at a distance lower than 15 Å were considered for these calculations. For the case of the hexagonal structure, just first neighbors are captured with the above mentioned cutoff for the CTI. For the case of the concave-convex structure, up to the third neighbors are included in the CTI calculations (see Fig. 3). Note that the shortest distances between the walls of [8]CPPs oscillates around 3.1–3.4 Å

The distribution of CTI for the hexagonal structure, shown in Fig. 6, presents similar values for electron and hole transfer integrals. The mean value for t_h is 48 meV, which is slightly higher than the mean value for t_e of 30 meV, as well as its standard

deviation (σ_h = 34 meV, σ_e = 23 meV, respectively). The CTI values obtained for the hexagonal structure lie in a broad range from 1 to 150 meV, which agrees with the trends shown in Figs. 4a–4c. To explain this distribution, we calculated the orientation of a CPP molecule in the monolayer using the variation of the orientation of the vector (**d**) formed between the center of mass of the molecule and a specific carbon atom in the bridge between two phenyl units, i.e. the ring. At the beginning of the simulation, the initial configuration is a perfect replica of the hexagonal unit cell. At the end of the simulation, the angle formed between the new vector (**d'**) and the initial one (**d**) spans a range of 15 degrees (from $-7°$ to $7°$). These apparently small rotations of one molecule with respect to another can actually strongly affect the CTI values, as highlighted by Fig. 4b, and leads to a broad distribution of transfer integral values.

A more complex behavior is obtained for the concave-convex structure, for which different neighbors exist depending on the crystallographic direction. The CTI values are shown in Fig. 7, with the contributions for each neighbor plotted separately. The tubular configuration that corresponds to the second neighbors presents negligible CTIs. This result can be explained by invoking Fig. 4d, since second neighbors are at distances comprised between 9 to 11 Å and thus CTIs tend to zero. Even if (hypothetically) the tubular configuration in the HB structure on graphite were found to be identical to the one in the tridimensional crystal, these CTI would be low, as we show in Fig. 4e, since electron couplings are sizable just in the case of perfectly aligned tubular structure. Conversely, much larger contributions from first and third neighbors are found. The concave-convex configuration, that corresponds to the first neighbors, presents mean values of CTI for holes and electrons of 6 and 10 meV, and σ_h and σ_e of 4 and 8 meV, respectively. For the third neighbors, mean values for t_h and t_e are surprisingly rather large: 5 and 16 meV, with σ_h and σ_e of 2 and 7 meV, respectively.

3.5 Charge-transport rates and mobilities

Charge-transport rates were calculated from Eq. (1) at a temperature of 300 K, with values for λ taken from Ref. [39] (281 and 302 meV for hole and electron, respectively). For the hexagonal structure, k_h and k_e are calculated to be comprised between 2×10^9 – 5×10^{13} s^{-1} and 4×10^8 – 2×10^{13} s^{-1}, respectively, considering the lower and higher values obtained for the CTI. For the concave-convex structure, k_h and k_e values range between 2×10^7 – 6×10^{11} s^{-1} and 2×10^7 – 2×10^{12} s^{-1}, respectively, to be again considered as the lower and upper values. To put these values in the context of organic charge transport, it is useful to compare the rates on [8]CPP monolayers with those calculated for some well-known organic molecular semiconductors (e.g. pentacene and rubrene): k_h and h_e were calculated for a perfect array of cofacial pentacenes to be 3×10^{14} s^{-1} and 1×10^{14} s^{-1}.[61] Slightly smaller values are found in the crystalline structure of pentacene and rubrene, with values of k_h around 1×10^{14} s^{-1},[62] but in both cases these materials benefit from much lower values for λ than those found for [8]CPP. Actually, since the reorganization energies decrease for longer CPPs compared with [8]CPP, e.g. they are about 30% smaller for the case of [12]CPP vs [8]CPP, one could anticipate better charge-transport performances for longer rings if all other factors affecting the mobility remain unchanged.

Note also how mobility for the hexagonal structure is expected to be isotropic in all in-plane directions, which differentiates CPPs from other planar (i.e. lath-shaped) organic semiconductors such as oligoacenes. To demonstrate this effect, we also calculated the angular dependence of the mobility for both hexagonal and concave-convex cases with equations 3 and 4. Figure 8 shows the in-plane mobilities for holes and electrons, with maximum values of 5.6 and 1.7 cm^2 V^{-1} s^{-1} for hexagonal (or 0.06 and 0.32 cm^2 V^{-1} s^{-1} for concave-convex) configuration, respectively. A quantitative comparison with rubrene and pentacene, for which hole mobilities of 23 and 20 cm^2 V^{-1} s^{-1} are predicted employing the same methodology, suggest that hexagonal monolayers of [8]CPPs could be exploited as 2D semiconductors.

4 Conclusions

Computer simulations were used to predict self-assembling of thin-films of [8]CPPs on graphite surfaces, and to establish the structure-property relationship for charge transport phenomena. A tailored force field was derived and shown to be able to reasonably reproduce the molecular structure of an isolated [8]CPP, as well as adsorption energy curves and the crystalline structure of model interactions, proving that a detailed description of molecular aggregation of CPPs on graphitic surfaces can be simulated from scratch. The monolayer growth was studied for the case of [8]CPPs adsorbed in horizontal configuration, observing a self-aggregation in a hexagonal pattern. The corresponding aggregation of molecules in vertical configuration was found unstable both at partial coverage and in full coverage simulations. However, a new full-coverage structure in the vertical configuration has been proposed, based in the herringbone structure experimentally observed in bulk crystals.

Additionally, the charge transport properties were evaluated in both structures, leading to the conclusion that the hexagonal configuration presents higher electronic couplings than the concave-convex structure, which readily translates into larger charge-transfer rates and mobility for both holes and electrons. Overall, our simulations offer detailed information about structural and electronic properties of physisorbed cyclic nanorings, suggesting that these materials could be exploited for the realization of self-assembled semiconducting organic monolayers.

5 Acknowledgments

A.J.P.J. and J.C.S.G. acknowledge the project CTQ2014–55073-P from Spanish Government (MINECO/FEDER) and the project AICO/2018/175 from the Regional Government (GVA/FSE). L.M. acknowledges funding from MIUR–PRIN 2015XJA9NT (Molecular Organization in Organic Thin Films via Computer Simulation of their Fabrication Processes). We gratefully acknowledge useful discussions with Profs. Claudio Zannoni and Dr. Silvia Orlandi (University of Bologna, Italy). The dimer

projection and orthonormalization was calculated using a in-house script kindly provided by Dr. Gabriele D'Avino (Néel Institute, Grenoble).

References

[1] Lewis, S. E. *Chem. Soc. Rev.* **2015**, *44*, 2221–2304.

[2] Wu, D.; Cheng, W.; Ban, X.; Xia, J. *Asian J. Org. Chem.* **2018**, *7*, 1–22.

[3] Darzi, E. R.; Jasti, R. *Chem. Soc. Rev.* **2015**, *44*, 6401–6410.

[4] Kayahara, E.; Sun, L.; Onishi, H.; Suzuki, K.; Fukushima, T.; Sawada, A.; Kaji, H.; Yamago, S. *J. Am. Chem. Soc.* **2017**, *139*, 18480–18483.

[5] Iwamoto, T.; Watanabe, Y.; Sadahiro, T.; Haino, T.; Yamago, S. *Angew. Chem. Int. Ed.* **2011**, *50*, 8342–8344.

[6] Xia, J.; Bacon, J. W.; Jasti, R. *Chem. Sci.* **2012**, *3*, 3018.

[7] Segawa, Y.; Omachi, H.; Itami, K. *Org. Lett.* **2010**, *12*, 2262–2265.

[8] Franke, J.; Vögtle, F. *Tetrahedron Lett.* **1984**, *25*, 3445–3448.

[9] Friederich, R.; Nieger, M.; Vögtle, F. *Chem. Ber.* **1993**, *126*, 1723–1732.

[10] Jasti, R.; Bhattacharjee, J.; Neaton, J. B.; Bertozzi, C. R. *J. Am. Chem. Soc.* **2008**, *130*, 17646–17647.

[11] Tabaka, H.; Omachi, H.; Yamamoto, Y.; Bouffard, J.; Itami, K. *Angew. Chem. Int. Ed.* **2009**, *48*, 6112–6116.

[12] Omachi, H.; Matsuura, S.; Segawa, Y.; Itami, K. *Angew. Chem. Int. Ed.* **2010**, *49*, 10202–10205.

[13] Yamago, S.; Watanabe, Y.; Iwamoto, T. *Angew. Chem. Int. Ed.* **2010**, *49*, 757–759.

[14] Xia, J.; Jasti, R. *Angew. Chem. Int. Ed.* **2012**, *51*, 2474–2476.

[15] Golder, M. R.; Jasti, R. *Acc. Chem. Res.* **2015**, *48*, 557–566.

[16] Segawa, Y.; Miyamoto, S.; Omachi, H.; Matsuura, S.; Šenel, P.; Sasamori, T.; Tokitoh, N.; Itami, K. *Angew. Chem. Int. Ed.* **2011**, *50*, 3244–3248.

[17] Segawa, Y.; Šenel, P.; Matsuura, S.; Omachi, H.; Itami, K. *Chem. Lett.* **2011**, *40*, 423–425.

[18] Fukushima, T.; Sakamoto, H.; Tanaka, K.; Hijikata, Y.; Irle, S.; Itami, K. *Chem. Lett.* **2017**, *46*, 855–857.

[19] Spisak, S. N.; Wei, Z.; Darzi, E.; Jasti, R.; Petrukhina, M. A. *Chem. Commun.* **2018**, *54*, 7818–7821.

[20] Pérez-Guardiola, A.; Pérez-Jiménez, A. J.; Sancho-García, J. C. *Mol. Sys. Des. Eng.* **2017**, *2*, 253–262.

[21] Sure, R.; Grimme, S. *J. Comput. Chem.* **2013**, *34*, 1672–1685.

[22] Brandenburg, J. G.; Grimme, S. In *Prediction and Calculation of Crystal Structures: Methods and Applications*; Atahan-Evrenk, S., Aspuru-Guzik, A., Eds.; Springer International Publishing: Cham, 2014.

[23] Neese, F. *WIREs Comput. Mol. Sci.* **2012**, *2*, 73–78.

[24] Becke, A. D. *J. Chem. Phys.* **1993**, *98*, 5648–5652.

[25] Kendall, R. A.; Dunning, T. H.; Harrison, R. L. *J. Chem. Phys.* **1992**, *96*, 6796–6806.

[26] Frisch, M. J.; Pople, J. A.; Binkley, J. S. *J. Chem. Phys.* **1984**, *80*, 3265–3269.

[27] M. J. Frisch, G. W. Trucks, H. B. Schlegel, G. E. Scuseria, M. A. Robb, J. R. Cheeseman, G. Scalmani, V. Barone, B. Mennucci, G. A. Petersson, H. Nakatsuji, M. Caricato, X. Li, H. P. Hratchian, A. F. Izmaylov, J. Bloino, G. Zheng, J. L. Sonnenberg, M. Hada, M. Ehara, K. Toyota, R. Fukuda, J. Hasegawa, M. Ishida, T. Nakajima, Y. Honda, O. Kitao, H. Nakai, T. Vreven, J. A. Montgomery, Jr., J. E. Peralta, F. Ogliaro, M. Bearpark, J. J. Heyd, E. Brothers,

K. N. Kudin, V. N. Staroverov, R. Kobayashi, J. Normand, K. Raghavachari, A. Rendell, J. C. Burant, S. S. Iyengar, J. Tomasi, M. Cossi, N. Rega, J. M. Millam, M. Klene, J. E. Knox, J. B. Cross, V. Bakken, C. Adamo, J. Jaramillo, R. Gomperts, R. E. Stratmann, O. Yazyev, A. J. Austin, R. Cammi, C. Pomelli, J. W. Ochterski, R. L. Martin, K. Morokuma, V. G. Zakrzewski, G. A. Voth, P. Salvador, J. J. Dannenberg, S. Dapprich, A. D. Daniels, Ö. Farkas, J. B. Foresman, J. V. Ortiz, J. Cioslowski, and D. J. Fox, Gaussian 09 (Gaussian, Inc., Wallingford CT, 2009).

[28] Singh, U. C.; Kollman, P. A. *J. Comput. Chem.* **1984**, *5*, 129–145.

[29] Cornell, W. D.; Cieplak, P.; Bayly, C. I.; Gould, I. R.; Merz, K. M.; Ferguson, D. M.; Spellmeyer, D. C.; Fox, T.; Caldwell, J. W.; Kollman, P. A. *J. Am. Chem. Soc.* **1995**, *117*, 5179–5197.

[30] Essman, U.; Perera, L.; Berkowitz, M. L.; Darden, T.; Lee, H.; Pedersen, L. G. *J. Chem. Phys.* **1995**, *103*, 8577–8593.

[31] Berendsen, H. J. C.; Postma, J. P. M.; van Gunsteren, W. F.; Nola, A. D.; Haak, J. R. *J. Chem. Phys.* **1984**, *81*, 3684–3690.

[32] Phillips, J. C.; Braun, R.; Wang, W.; Gumbart, J.; Tajkhorshid, E.; Villa, E.; Chipot, C.; Skeel, R. D.; Kalé, L.; Schulten, K. *J. Comput. Chem.* **2005**, *26*, 1781–1802.

[33] Hassel, O. *Z. Phys.* **1924**, *25*, 317–337.

[34] Marcus, R. A.; Sutin, N. *Biochim. Biophys. Acta* **1985**, *811*, 265–322.

[35] Brédas, J.-L.; Beljonne, D.; Coropceanu, V.; Cornil, J. *Chem. Rev.* **2004**, *104*, 4971–5004.

[36] Coropceanu, V.; Cornil, J.; da Silva Filho, D. A.; Olivier, Y.; Silbey, R.; Brédas, J.-L. *Chem. Rev.* **2007**, *107*, 926–952.

[37] Stehr, V.; Fink, R. F.; Tafipolski, M.; Deibel, C.; Engels, B. *WIREs Comput. Mol. Sci.* **2016**, *6*, 694–720.

[38] Oberhofer, H.; Reuter, K.; Blumberger, J. *Chem. Rev.* **2017**, *117*, 10319–10357.

[39] Sancho-García, J. C.; Moral, M.; Pérez-Jiménez, A. J. *J. Phys. Chem. C* **2016**, *120*, 9104–9111.

[40] Valeev, E.; Coropceanu, V.; da Silva Filho, D. A.; Salman, S.; Brédas, J.-L. *J. Am. Chem. Soc.* **2006**, *128*, 9882–9886.

[41] Kirkpatrick, J. *Int. J. Quantum Chem.* **2008**, *108*, 51–56.

[42] Baumeier, B.; Kirkpatrick, J.; Andrienko, D. *Phys. Chem. Chem. Phys.* **2010**, *12*, 11103–11113.

[43] Löwdin, P. *J. Chem. Phys.* **1950**, *18*, 365–375.

[44] Kubas, A.; Hoffmann, F.; Heck, A.; Oberhofer, H.; Elstner, M.; Blumberger, J. *J. Chem. Phys.* **2014**, *140*, 104105.

[45] Kubas, A.; Gajdos, F.; Heck, A.; Oberhofer, H.; Elstner, M.; Blumberger, J. *Phys. Chem. Chem. Phys.* **2015**, *17*, 14342–14354.

[46] Chai, J.-D.; Head-Gordon, M. *J. Chem. Phys.* **2008**, *128*, 084106.

[47] Sutton, C.; Sears, J. S.; Coropceanu, V.; Brédas, J.-L. *J. Phys. Chem. Lett.* **2013**, *4*, 919–924.

[48] Stehr, V.; Pfister, J.; Fink, R. F.; Engels, B.; Deibel, C. *Phys. Rev. B* **2011**, *83*, 155208.

[49] Pettersen, E. F.; Goddard, T. D.; Huang, C. C.; Couch, G. S.; Greenblatt, D. M.; Meng, E. C.; Ferrin, T. E. *J. Comput. Chem.* **2004**, *25*, 1605–1612.

[50] Macrae, C. F.; Bruno, I. J.; Chisholm, J. A.; Edgington, P. R.; McCabe, P.; Pidcock, E.; Rodriguez-Monge, L.; Taylor, R.; van de Streek, J.; Wood, P. A. *J. Appl. Cryst.* **2008**, *41*, 466–470.

[51] Humphrey, W.; Dalke, A.; Schulten, K. *J. Mol. Graphics* **1996**, *14*, 33–38.

[52] Hunter, J. D. *Comp. Sci. Eng.* **2007**, *9*, 90–95.

[53] Olivier, Y.; Muccioli, L.; Zannoni, C. *ChemPhysChem* **2014**, *15*, 1345–1355.

[54] Jorgensen, W. L.; Maxwell, D. S.; Tirado-Rives, J. *J. Am. Chem. Soc.* **1996**, *118*, 11225–11236.

[55] Sancho-García, J. C. *J. Chem. Phys.* **2006**, *124*, 124112.

[56] Climent-Medina, J.-V.; Pérez-Jiménez, A.-J.; Moral, M.; San-Fabián, E.; Sancho-García, J.-C. *ChemPhysChem* **2015**, *16*, 1520–1528.

[57] Grimme, S.; Ehrlich, S.; Goerigk, L. *J. Comput. Chem.* **2011**, *32*, 1456–1465.

[58] Reche-Tamayo, M.; Moral, M.; Pérez-Jiménez, A. J.; Sancho-García, J. C. *J. Phys. Chem. C* **2016**, *120*, 22627–22634.

[59] Moral, M.; Son, W.-J.; Sancho-García, J. C.; Olivier, Y.; Muccioli, L. *J. Chem. Theory Comput.* **2015**, *11*, 3383–3392.

[60] Brédas, J. L.; Calbert, J. P.; da Silva Filho, D. A.; Cornil, J. *Proc. Natl. Acad. Sci.* **2002**, *99*, 5804–5809.

[61] Olivier, Y.; Lemaur, V.; Brédas, J. L.; Cornil, J. *J. Phys. Chem. A* **2006**, *110*, 6356–6364.

[62] Kobayashi, H.; Kobayashi, N.; Hosoi, S.; Koshitani, N.; Murakami, D.; Shirasawa, R.; Kudo, Y.; Hobara, D.; Tokita, Y.; Itabashi, M. *J. Chem. Phys.* **2013**, *139*, 014707.

Table 1: Interacting energy (kcal/mol) of different dimers extracted from the crystalline structure[6] at different levels. The figures show two different [h k l] planes. (a) and (b) refer to the two different crystalline planes shown.

(a) (b)

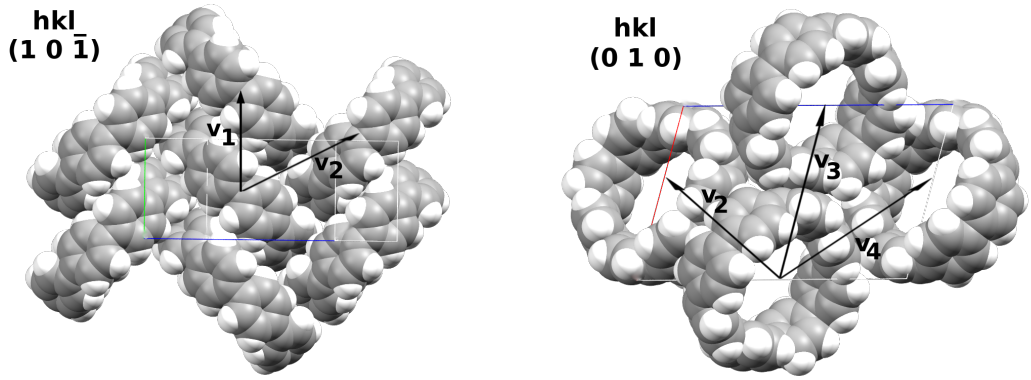

	crystal vector	B3LYP-D3(BJ)	HF-3c	FF
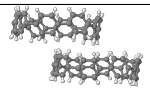	$\mathbf{v}_1$ (0, 1, 0)	-14.04	-11.61	-12.76
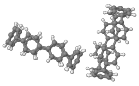	$\mathbf{v}_2$ ($\frac{1}{2}$, $\frac{1}{2}$, $\frac{1}{2}$)	-10.72	-9.66	-9.86
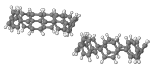	$\mathbf{v}_3$ (1, 0, 0)	-10.40	-9.04	-9.00
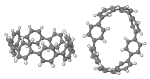	$\mathbf{v}_4$ (-$\frac{1}{2}$, $\frac{1}{2}$, $\frac{1}{2}$)	-6.42	-5.77	-5.76

Table 2: Comparison between experimental and simulated unit cell dimensions at 300 K and 1 bar of pressure.

	a (Å)	b (Å)	c (Å)	α (°)	β (°)	γ (°)	ρ (g/cm^3)
Experimental	12.933	8.010	19.368	90	105.363	90	1.045
Simulated	12.957	7.938	19.111	90	105.598	90	1.068

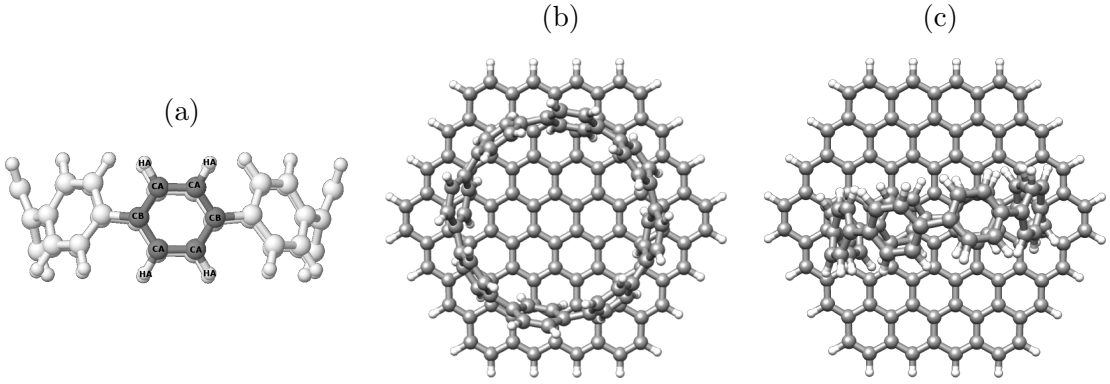

Figure 1: (a) Ball-and-sticks chemical structure of the [8]cycloparaphenylene ([8]CPP) molecule, with labels corresponding to the atom types employed in force field parameterization and simulations. (b)–(c) Top views of the weakly bond [8]CPP$\cdots C_{96}H_{24}$ systems for both configurations studied.

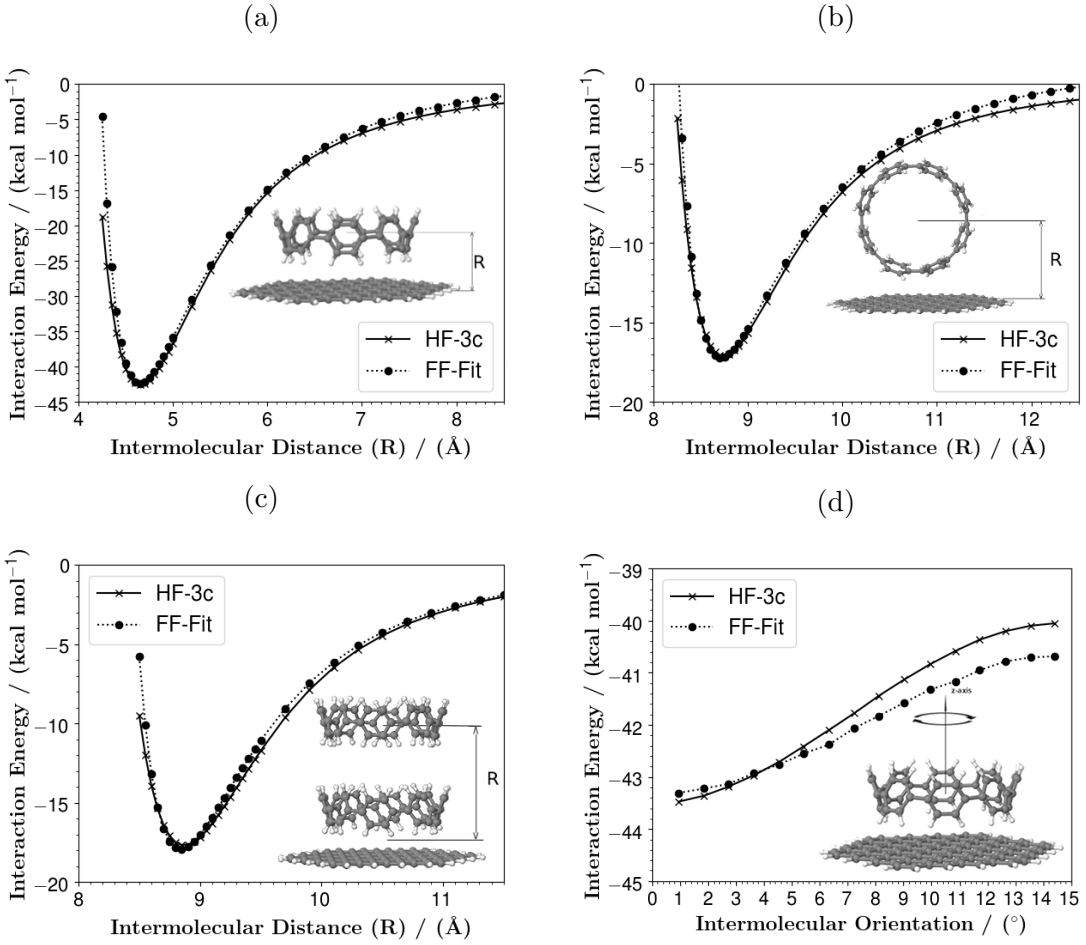

Figure 2: Potential energy curves of [8]CPP interacting with finite-size graphene nano-flakes (17.44Å×15.73Å) in different configurations. The dotted lines correspond to the interaction energy obtained from the parameterized force field. HF-3c potential energy curves were obtained from Ref. [20], except the curve 2c calculated here.

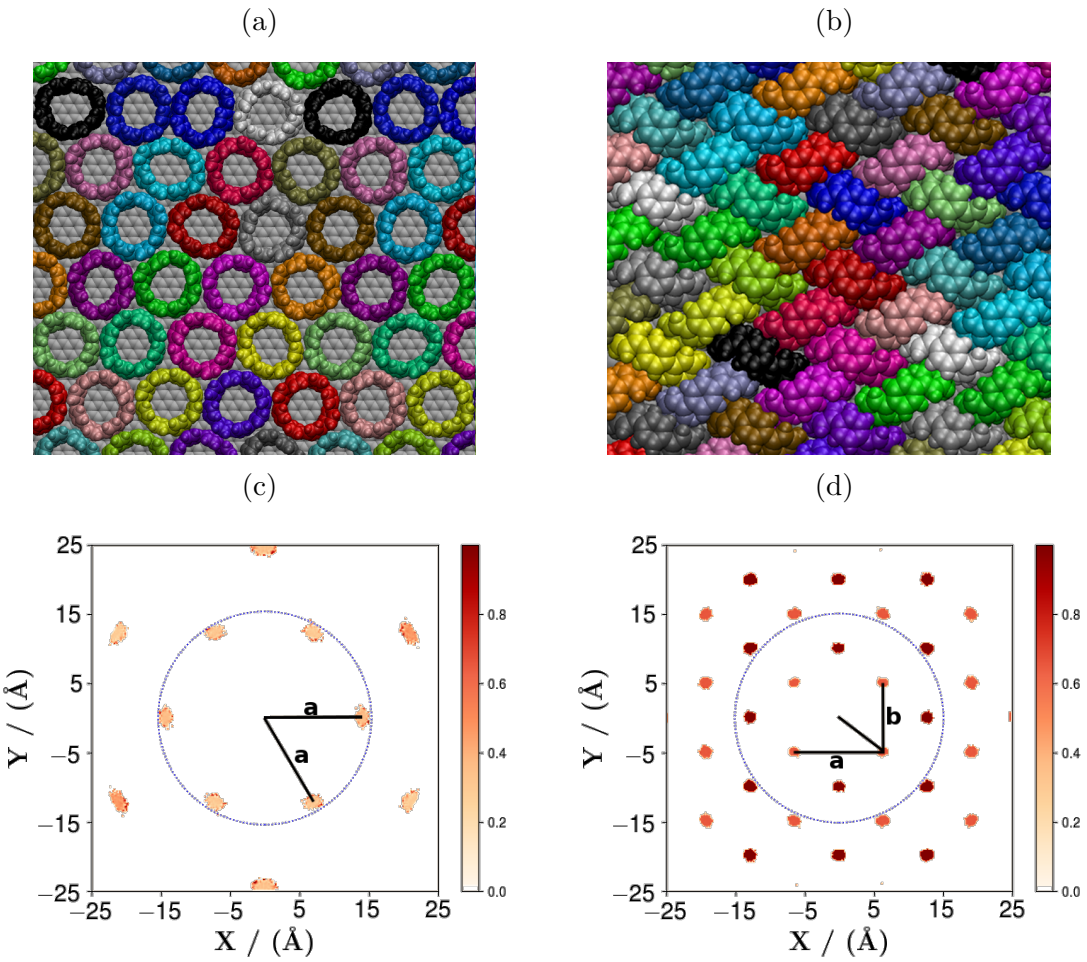

Figure 3: [8]CPP monolayers at complete coverage on graphite. (a) Hexagonal structure of horizontal molecules; and (b) rectangular structure of vertical, concave-convex arranged molecules. In-plane radial pair distributions (c) and (d) for hexagonal and concave-convex adlayers, respectively, with segments representing the lattice vectors. The dotted line represent the cutoff for the evaluation of the CTIs. This quantity gives the probability of finding a neighbouring [8]CPP molecule at a given position on the plane, when the reference molecule is fixed at the origin.

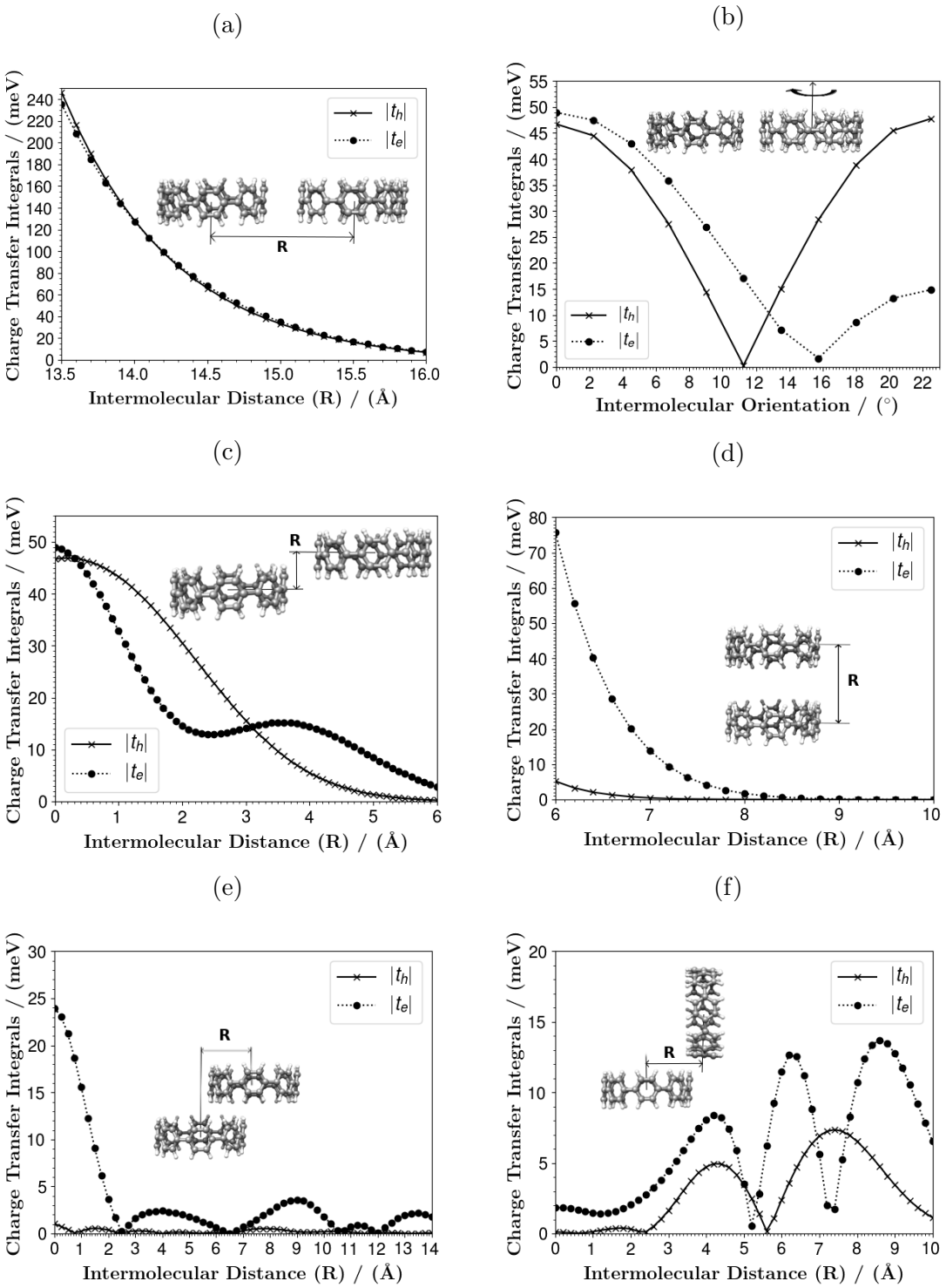

Figure 4: The dependence of charge transfer integrals on relative distances and orientations between weakly interacting [8]CPP systems.

(a) [8]CPP HOMO

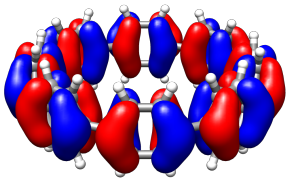

(b) [8]CPP LUMO

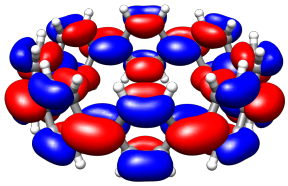

(c) cofacial HOMO (ψ^-)

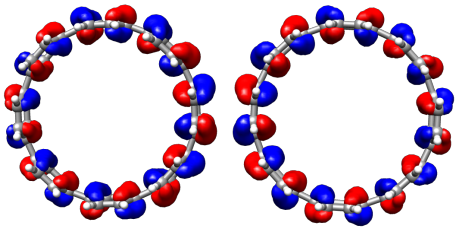

(d) cofacial LUMO (ψ^+)

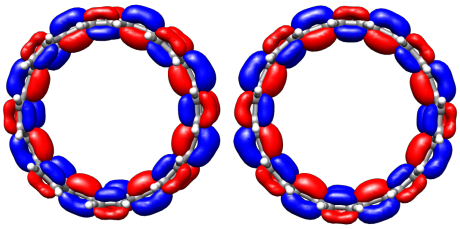

(e) tubular HOMO (ψ^-)

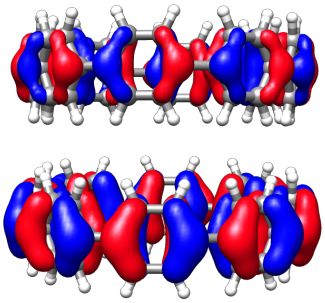

(f) tubular LUMO (ψ^+)

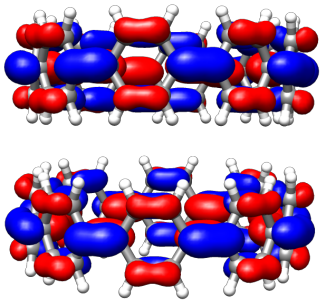

Figure 5: Isocontour plots of the (a) HOMO and (b) LUMO orbitals of an isolated [8]CPP molecule, as well as their counterparts for dimers in two model configurations: (c)–(d) cofacial and (e)–(f) tubular. The size and color described the amplitude and sign, respectively, of the lobes of orbitals.

(a)

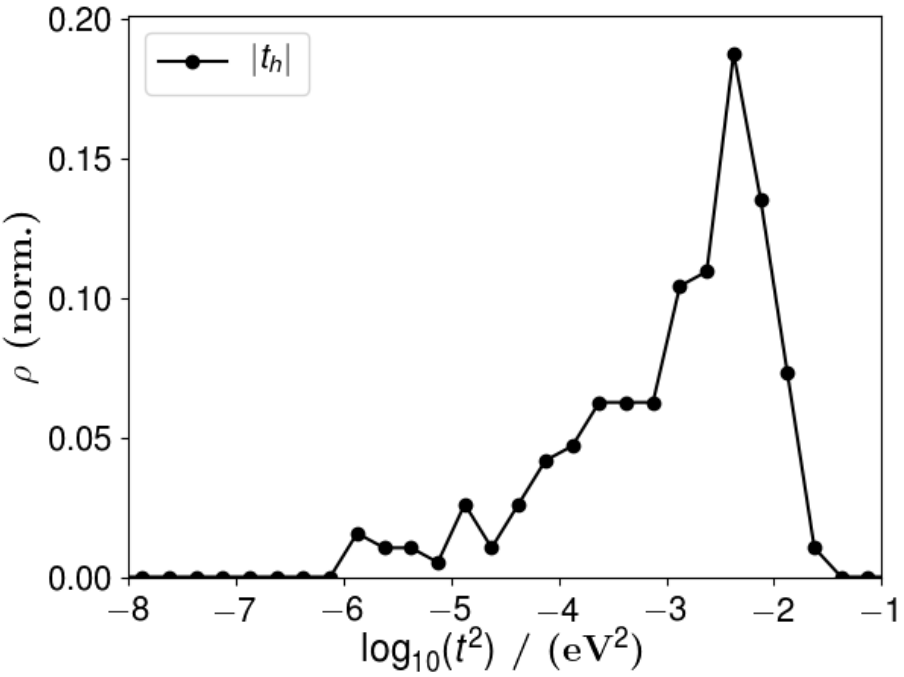

(b)

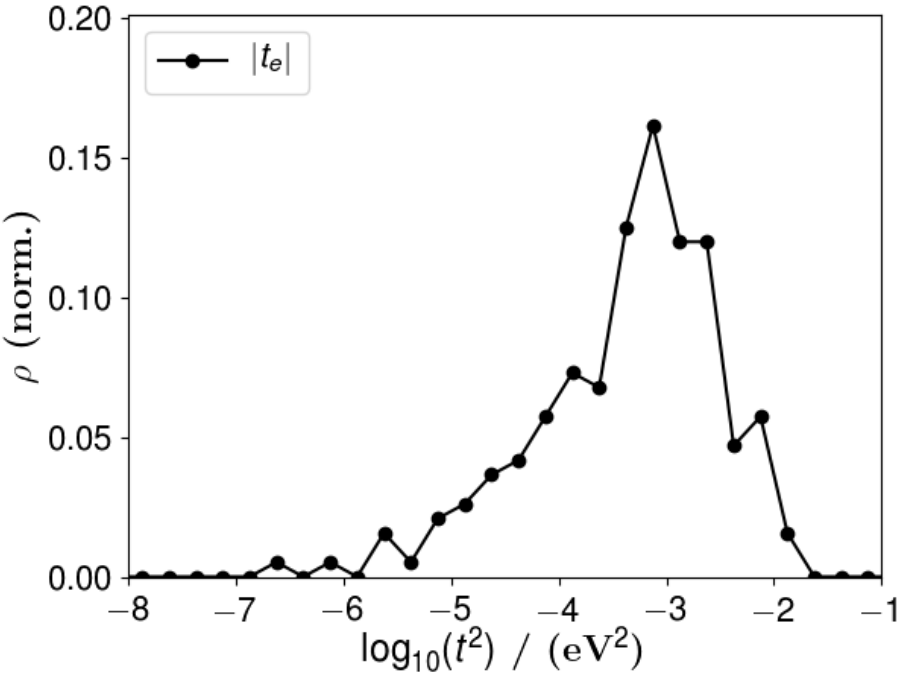

Figure 6: Charge transfer integrals distribution for (a) holes and (b) electrons in the hexagonal structure. All dimers considered were extracted from a snapshot from the full-coverage molecular dynamics simulation using a cutoff of 15 Å.

(a)

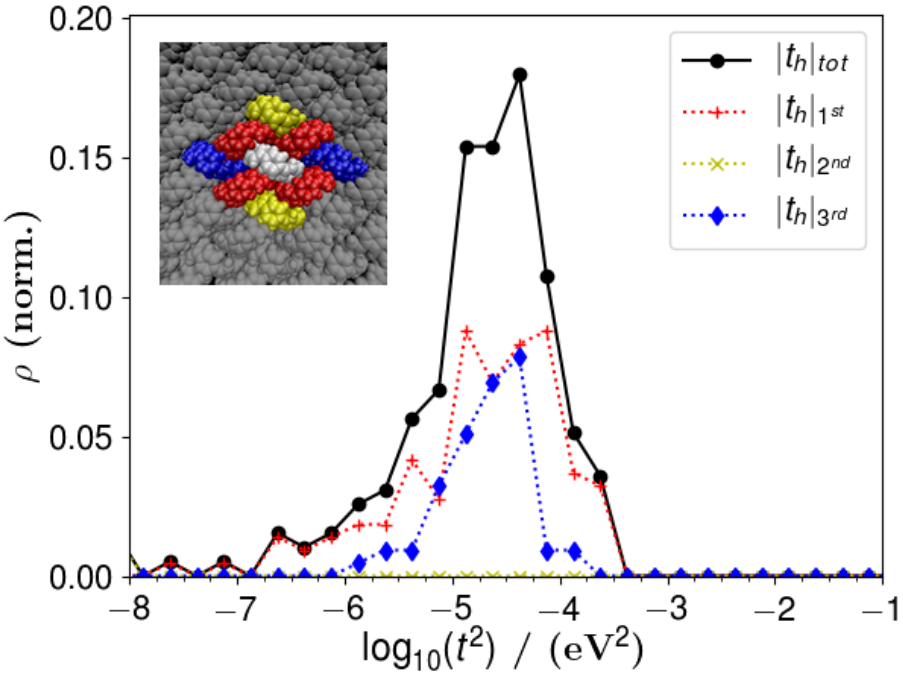

(b)

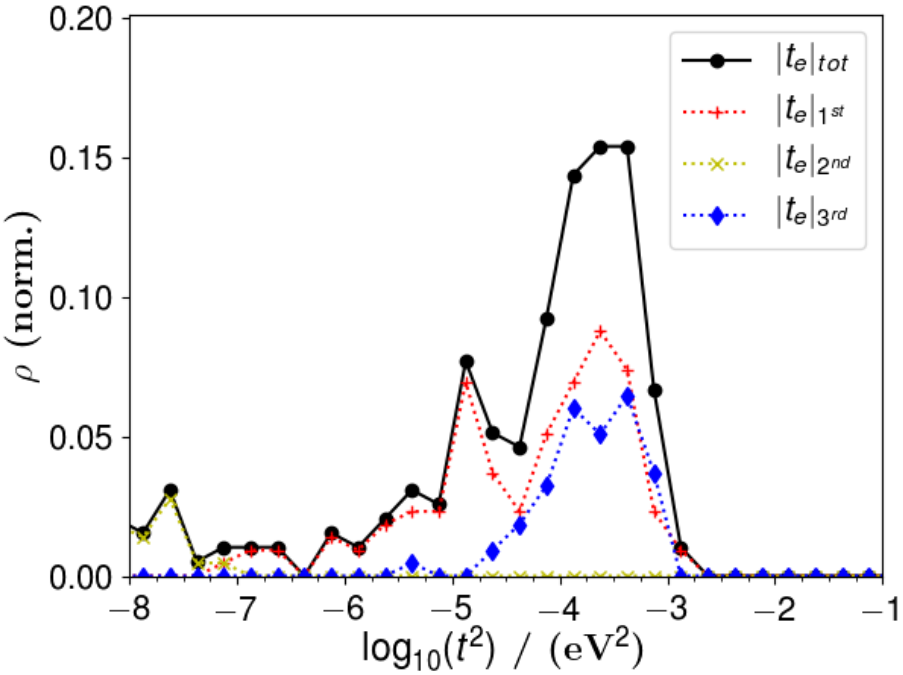

Figure 7: Charge transfer integrals distribution for (a) holes and (b) electrons in the concave-convex structure. Interacting dimers were considered until third neighbors (as shown in the inset of Fig. 7a, with first, second, and third neighbors represented with the same color code used in the plots) and their individual contributions are plotted separately.

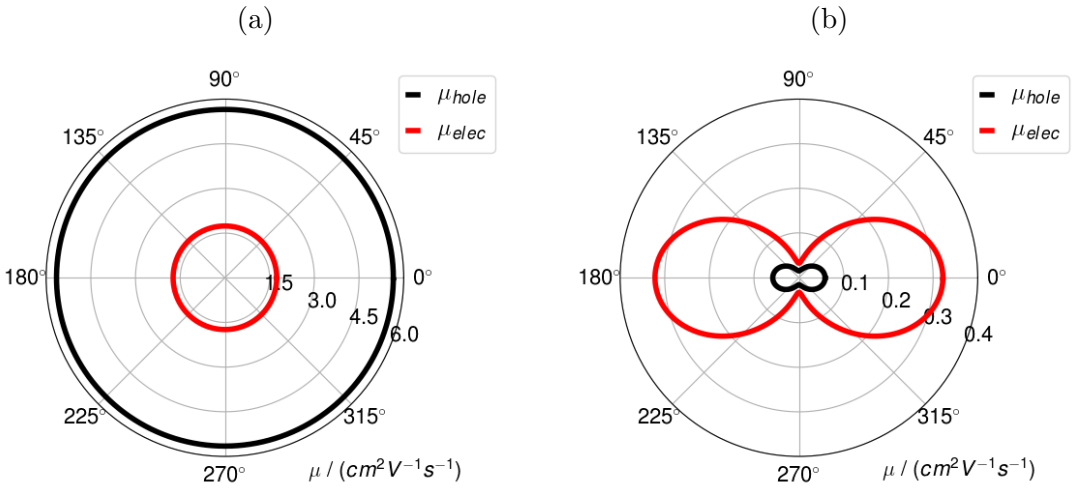

Figure 8: Comparison of the mobility for hexagonal (left) and concave-convex (right) configurations, and for both holes (black) and electrons (red). Note the different scale of absolute values in the two plots.

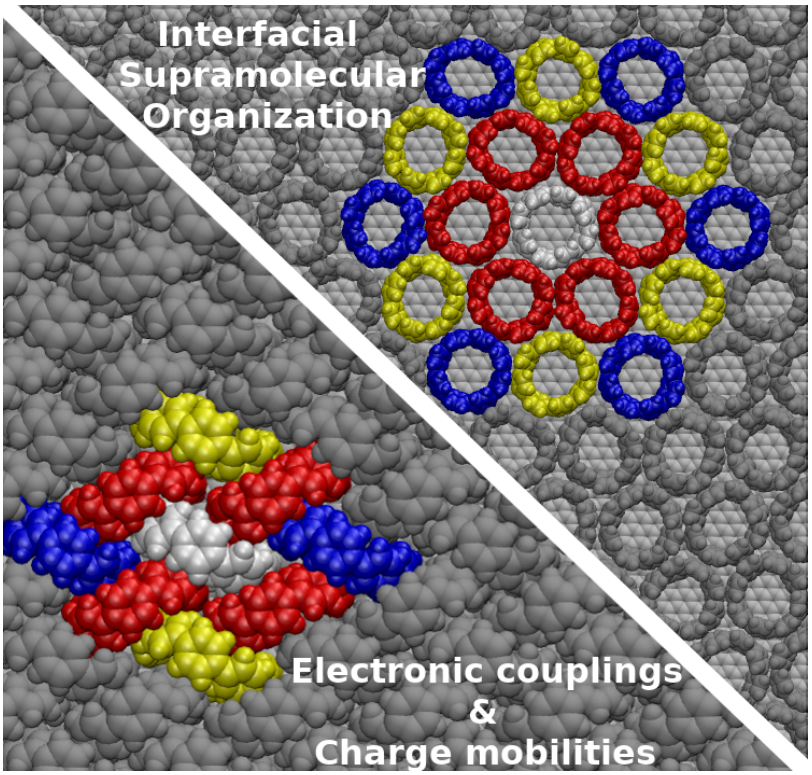

Figure 9: Graphical abstract